In-situ anisotropic growth of nickel oxide nanostructures

through layer-by-layer metal oxidation

Boyi Qu and Klaus van Benthem*

Department of Materials Science and Engineering, University of California Davis, 1 Shields

Ave, Davis, CA 95616, USA

* Corresponding author; email: benthem@ucdavis.edu

Abstract:

This study reports the one-directional growth of single crystalline nickel oxide nanostructures

that is facilitated by the oxidation of nickel nanoparticles. Layer-by-layer growth at the buried

NiO/Ni interface was directly observed by in-situ high resolution transmission electron

microscopy at 650°C in an oxygen partial pressure around 4x10⁻⁴ Pa. Individual layers of NiO

grow by ledge movement, i.e., disconnection migration along the oxide/metal interface plane.

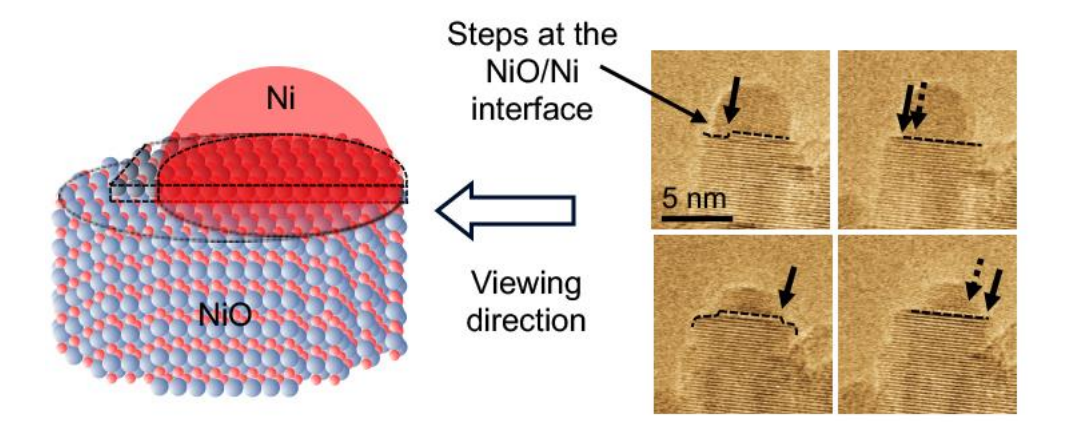
Oxidation at interfacial steps is governed by oxygen vacancy migration along the interface plane,

while the junction between the oxide/metal interface and the gas phase serves as nucleation site.

The results of this study demonstrate the applicability of the terrace-ledge-kink crystal growth

model for reactive crystal growth processes at internal heterophase interfaces.

1



Key words: oxidation; crystal growth; in-situ transmission electron microscopy; interfaces

One-dimensional nanostructures such as nanotubes, nanowires, and nanorods hold promise for a variety of applications owing to their exciting physical properties that can be considerably different compared to their bulk counterparts [1–5]. For their synthesis directional crystal growth strategies are reported [6–10] and include vapor-liquid-solid (VLS) [6], solution-liquid-solid (SLS) [7], and vapor-solid-solid (VSS) [8] mechanisms. These techniques leverage catalyst particles that serve as solvent and promote crystal growth by re-precipitation of the solute at the catalyst/nanostructure interface. The morphology and size of resulting nanostructures typically depend on the size of the catalyst particles [11]. However, controlling the growth process and management of dopant distributions however remains challenging during catalytic chemical vapor deposition. For instance, Oh and co-workers observed unwanted supersaturation of Au point defects in VLS grown silicon nanowires [12]. Kossel [13] and Stranski [14] originally introduced the terrace ledge-kink (TLK) model as a thermodynamic description of surface transformations during crystal growth. For VLS growth Hofmann and co-workers have subsequently demonstrated ledge propagation at the Pd silicide/Si interface during Si nanowire

growth in disilane atmosphere [15]. Ledge movement occurs by re-precipitation of Si from the silicide phase. The Burton-Cabrera-Frank screw dislocation growth model [9,10] utilizes the TLK formalism to describe crystal growth under low supersaturation. Self-perpetuating steps are formed from screw dislocation intersecting with the free surface [9,10]. The model was experimentally confirmed by a series of nanowire growth studies for different materials systems [16–18]. For metal oxide growth, adatoms from the gas phase are attached to step edges while screw dislocations within the growing nanostructure or oxide scale provide diffusion pathways for reactants [19,20].

Gleiter [21] adopted the terrace ledge kink mechanism to describe grain boundary migration during the recrystallization of Al-Cu alloys. Atoms are emitted from steps on the shrinking grain and added to the growing grain. Several authors have subsequently utilized the concept of disconnections, i.e., defects at grain boundaries with step and dislocation character [22] to describe grain boundary kinetics in oxide ceramics [23–27]. Zou et al. documented step movement during solid state reactions at curved metal/oxide interfaces [28]. However, interface curvature may have represented an additional driving force for interface migration [28]. This study provides direct evidence for reactive layer-by-layer growth of nickel oxide at a buried and atomically flat Ni/NiO interface. While anisotropic growth of nickel oxide nanostructures in water vapor was recently observed during in-situ environmental scanning electron microscopy [29], in-situ TEM experiments reported in the following demonstrate that the TLK model is also applicable to reactive crystal growth, including internal oxidation and oxide scale growth.

Anisotropic growth of NiO nanorods was carried out by in-situ heating of nickel nanoparticles (SkySpring Nanomaterials, Inc.) in an environmental scanning electron microscope (ESEM). Nanoparticles with a nominal diameter of 300 nm were dispersed in isopropanol and

drop-casted either onto thermally grown SiO₂ films supported by a silicon substrate, or a PELCO® Silicon Dioxide Support Film for TEM with a 18nm thick SiO₂ membrane (Ted Pella, Inc.). ESEM heating was performed with a ThermoFisher Quattro Environmental Scanning Electron Microscope (Thermo Fisher Scientific, Hillsboro, OR) under water vapor with base pressures ranging between 250 Pa and 400 Pa. Nickel nanoparticles were heated to 800 °C at a rate of 30-50 °C/min. The temperature was held at 800 °C for up to 45 minutes until no more morphological changes of the nickel nanoparticle agglomerates were detected. After ESEM heating bright field scanning transmission electron microscopy (STEM) imaging was carried out with a JEOL JEM 2100AC aberration corrected scanning transmission electron microscope. Energy dispersive X-ray spectroscopy (EDXS) line profiles were acquired with an Oxford Aztec Energy TEM Advanced Microanalysis System with an X-MaxN TSR Windowless large area Analytical Silicon Drift Detector.

Figure 1(a) reproduces earlier results of anisotropic growth of NiO nanostructures with a variety of different aspect ratios during ESEM heating at 800°C under 400 Pa of water vapor atmosphere [29]. Subsequent bright field STEM and conventional TEM imaging of as-grown high aspect ratio nanostructures reveal the absence (Figure 1(b)) or presence (Figure 1(c)) of metal nanoparticles at their tip. EDXS analysis (see Figure 1(d)) identified nanoparticle compositions as either pure Ni or Au-rich solid solutions of Cu and Au, which are impurities within the raw powder and were discussed previously [29] Similar matchstick-like morphologies of NiO nanostructures were previously documented by Koga and Hirasawa [30] after rapid oxidation of Ni-Au alloy nanoparticles above 600°C. The presence of Au-Cu nanoparticles at the tips of some NiO nanorods formed during ESEM heating is consistent with previously observed catalytic growth behavior [31,32]. However, many NiO nanostructures observed in this study

revealed either residual Ni particles (see (1) in Figure 1(c)) or no particles (Figure 1(b), which suggests an additional growth mechanism.

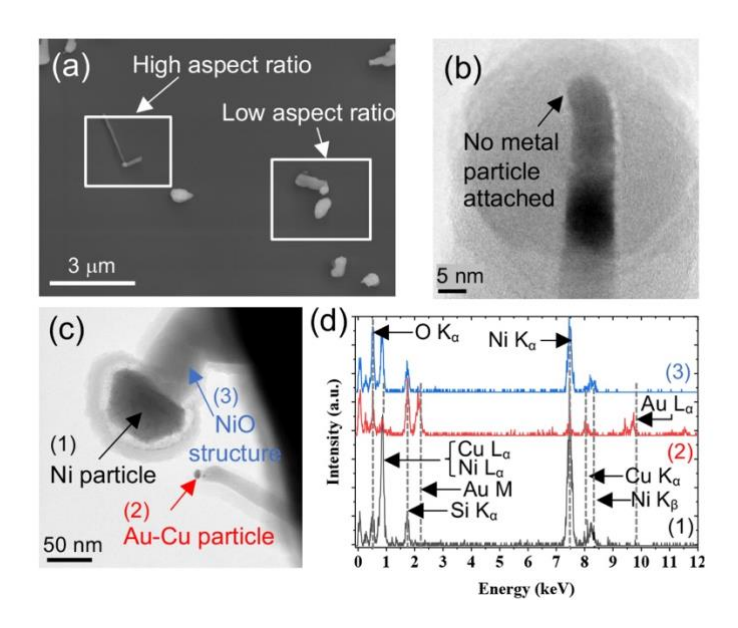


Figure 1. (a) SEM micrograph of nickel particles after ESEM heating at 800°C in 400 Pa of water vapor. Elongated nanostructures with different aspect ratios are observed. (b) & (c) STEM bright field images of three different nanostructures displaying the absence or presence of metal nanoparticles at their tips, respectively. (d) EDXS spectra recorded from metal nanoparticles labeled (1) and (2) in (c).

To interrogate atomic-scale growth mechanisms, in-situ high resolution transmission electron microscopy (HRTEM) heating experiments under simultaneous gas flow were carried out with a gas injection/specimen heating holder [33] inserted into a Hitachi HF-9500 transmission electron microscope operated at 300 kV. For these experiments Ni nanoparticles were formed by dewetting Ni thin films that were previously deposited onto thermally growth SiO2/Si substrates. Particle carrying substrates were crushed and deposited directly onto the tungsten heating wire of the in-situ sample holder. HRTEM images were recorded as video files while the tungsten wire

was resistively heated to 650 °C. Dry laboratory air was directed onto the TEM sample using a gas injection nozzle. During in-situ imaging the base pressure in the sample area was roughly $2x10^{-3}$ Pa. Figure 2 shows a series of HRTEM micrographs extracted from a video recorded during the nanostructure growth process (see online video file). After initial onset of NiO growth (see Figure 2(a) and (b)) the NiO/Ni interface becomes mostly flat for the remainder of the nanostructure growth. Dashed lines mark the interface between the growing NiO nanostructure and the shrinking Ni nanoparticle which is parallel to the (111) planes in both NiO and Ni. Throughout nanostructure growth lattice fringe contrast is observed from NiO and Ni indicating that both phases have remained solid and crystalline. The ratio of interplanar lattice spacings observed from the NiO nanorod and the Ni nanoparticle (cf. Figure 2(f)) is 1.2±0.1, which is consistent with the lattice constant ratio of 1.18 between NiO and Ni.

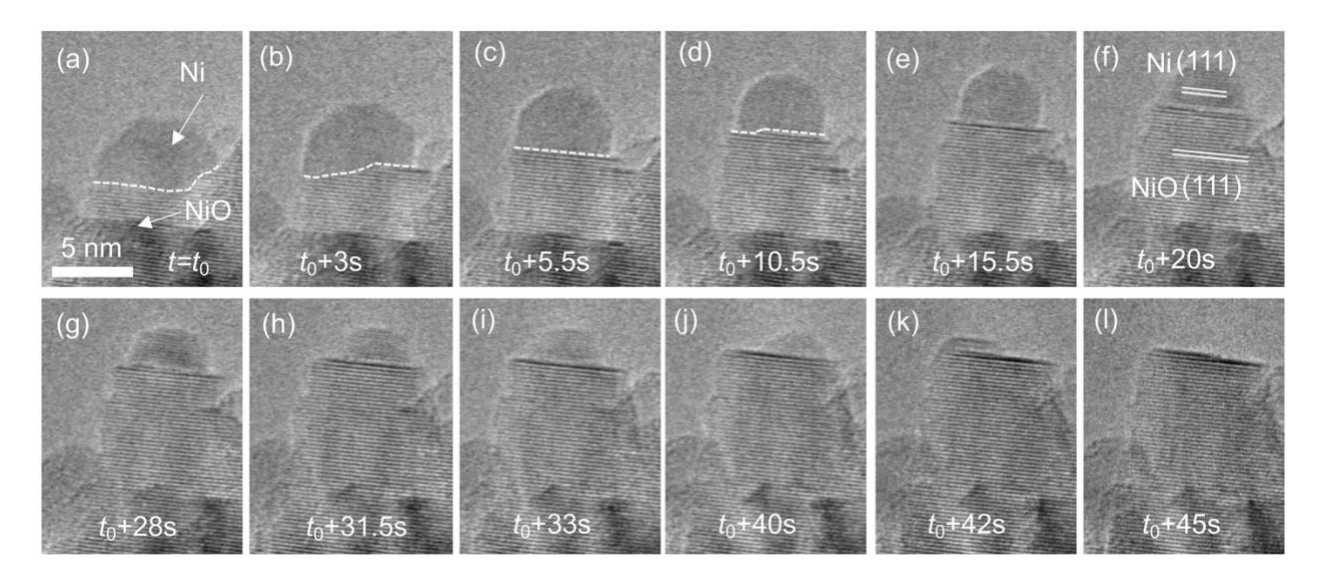


Figure 2: HRTEM micrographs extracted from an in-situ video recorded at 650 ℃ and a base pressure around 10⁻³ Pa. The NiO/Ni interface is marked by yellow dashed lines in (a)-(d). Time stamps are provided for each individual image. A single-crystalline NiO nanostructure grows in the

vertical direction while the crystalline nickel nanoparticle changes shape and reduces in size until fully consumed at t_0 +45s.

The change of the Gibbs free energy for oxide formation [34] suggests oxidation of metallic nickel under the in-situ TEM experimental conditions of 650°C and an oxygen partial pressure around 4x10⁻⁴ Pa. Consistent with previous observations of anisotropic growth of NiO nanostructures (cf. Figure 1 and [35]), Figure 2 therefore reveals that oxidation of Ni proceeds at the metal/oxide interface through layer-by-layer growth of NiO. The Ni nanoparticle shrinks (Figure 2(a)-(k)) by the subsequent removal of lattice planes until it is fully consumed by the reactive growth process (cf. Figure 2(1)) and NiO growth terminates. Figure 3 shows the appearance and subsequent disappearance of individual steps at the NiO/Ni interface at different times. Lattice planes grow by the movement of individual steps along the interface plane. Examples are highlighted by arrows in Figure 3 (a), (c), (e) and (g). New NiO lattice planes emerge from the side of the growing nanostructure, i.e., the NiO/Ni/gas phase junction. Similar to VLS growth of Si nanowires [36] these triple junctions serve as nucleation sites for NiO layer growth. Unexpectedly, the diameter of the growing nanorod remains unchanged during the continuous shrinkage of the Ni nanoparticle (Figure 2(f)-(k)). From this observation it is concluded that it is energetically more favorable for NiO to grow layer-by-layer instead of following a Stranski-Krastanov growth mode [14]. The movement of the metal nanoparticle on the oxide surface (Figure 2(g-k)) is likely a result of Ni surface diffusion during NiO growth, while the associated vacancy mechanism within the metal nanoparticle causes particle deformation and thus migration to continuously minimize free surface and interface energies. At the same time the Ni nanoparticle also changes its shape as a result of balancing its total surface energy with the NiO/Ni interface energy.

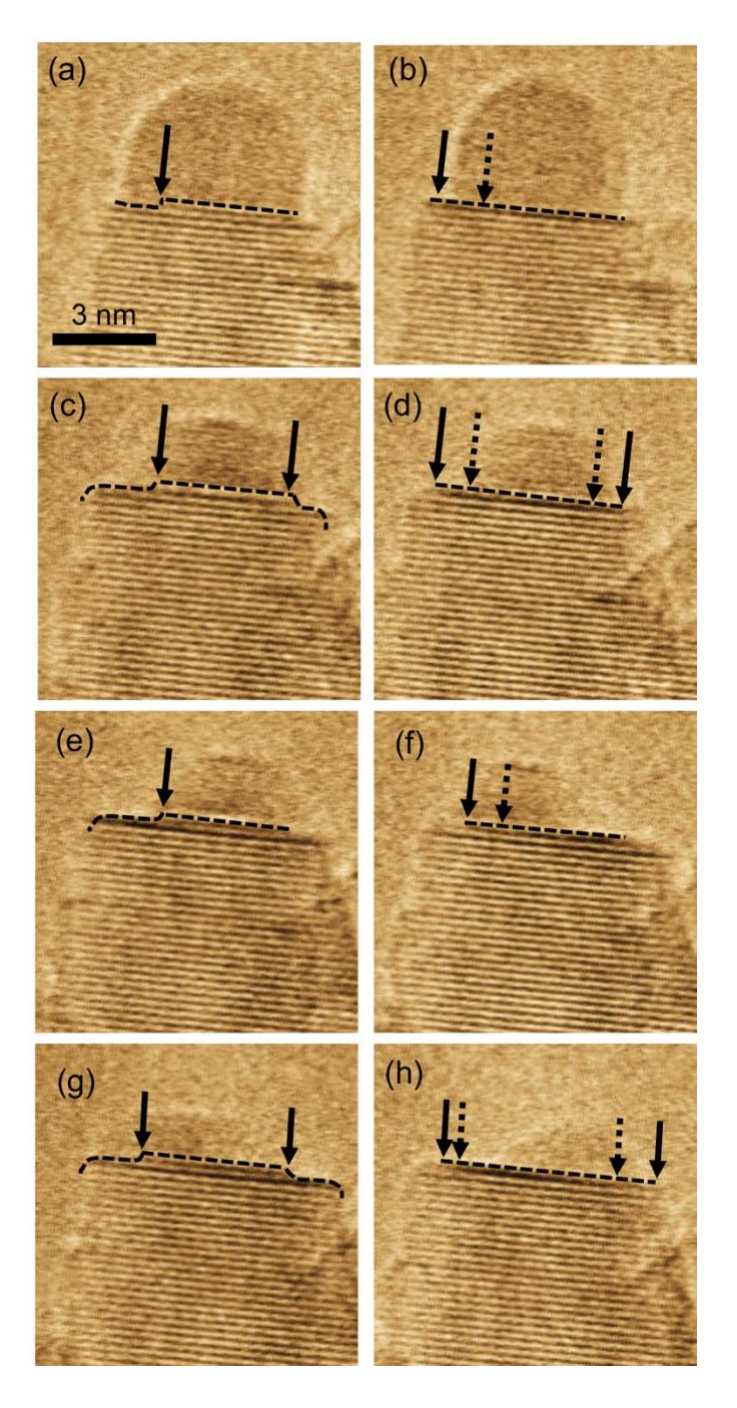


Figure 3. HRTEM images extracted from an in-situ video recorded at 650°C under 2x10⁻³ Pa of air. The images were rotated and intensities were color-coded for better presentation. Adjacent images (a&b, c&d, e&f, and g&h) represent subsequent video frames. The NiO/Ni interface is marked by the dashed lines. Steps at the interface are highlighted by arrows. The dashed arrows in (b) (d) (e) and (f) marks the step location in (a) (c) (f) and (g), respectively.

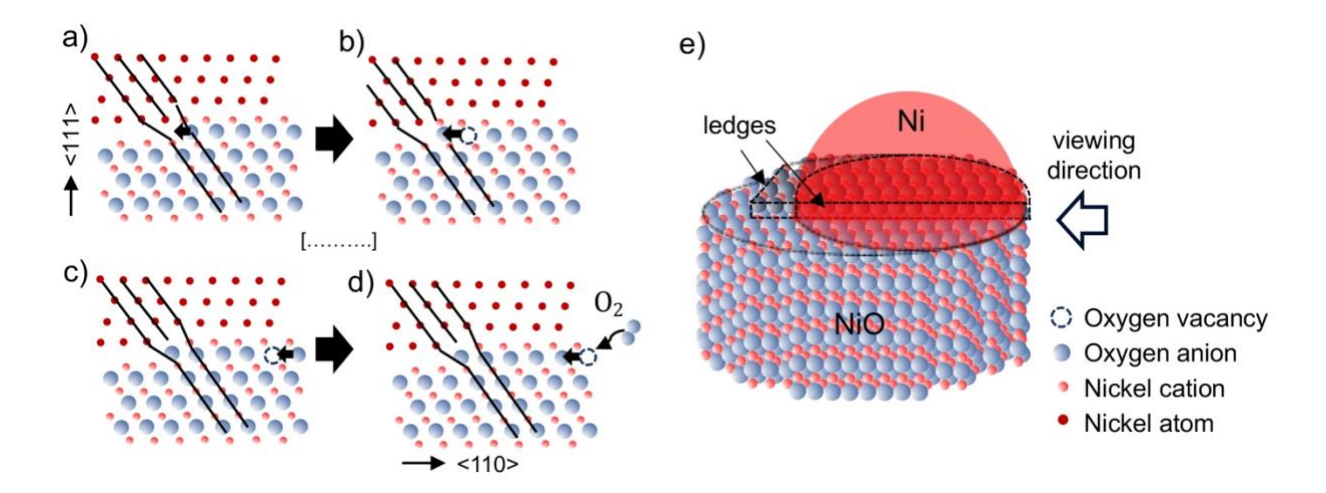


Figure 4. (a)-(d) 2D model of the NiO/Ni interface configuration representing the observed growth mechanism of NiO nanostructures. Misfit dislocations at the {111} NiO/Ni interface in conjunction with steps in the interface plane represent disconnections. Ledge movement is facilitated by oxygen vacancy diffusion along the interface plane which ensures oxygen supply for continuing oxidation of Ni atoms. (e) 3D representation of the shrinking Ni particle supported by the NiO surface with the viewing direction referring to the 2D projection views.

The NiO growth process observed in Figures 2 and 3 is sketched in Figure 4(a-d) for one possible crystal orientation with a {111} interface plane. Figure 4(e) is a 3D sketch representing the matchstick-like configuration of the NiO nanorod and the Ni particle with a possible viewing direction during the HRTEM experiments indicated by the black hollow arrow. The experimental observations in Figures 2 and 3 suggest that nickel oxidation occurs at kink sites along the NiO/Ni interface. The lattice mismatch between NiO and Ni is accommodated by misfit dislocations at the NiO/Ni interface (cf. Figure 4(a-d)). The layer-by-layer growth through the advancement of interfacial steps in the presence of misfit dislocations allows for the consideration of interface disconnections that facilitate the observed growth of NiO at the cost of

the shrinking Ni nanoparticle. This description is phenomenologically similar to the concept of mobile disconnections for the migration of grain boundaries in ceramics [22,24–27]. To advance a disconnection an interfacial nickel atom that is considered part of the metal nanoparticle bonds to an oxygen anion of the NiO surface (Figure 4(a)). At 650°C the thermodynamic driving force for oxidation is sufficient. As a result, oxygen migrates along the interface plane which advances the kink in the <110> direction for a {111} interface plane (cf. Figure 4(a) and 4(b)). As a result, an oxygen vacancy is created within the interfacial NiO plane which migrates along the interface (Figure 4(c)) towards the triple junction between the NiO/Ni interface and the gas phase (Figure 4(d)). This process enables oxygen anion supply from the gas phase for subsequent oxidation reactions to facilitate kink advancement. The in-situ HRTEM imaging results displayed in Figure 3 are consistent with such disconnection movement by anion-vacancy diffusion. Due to the 2D projection some interfacial steps may not be detected during HRTEM imaging while others may not necessarily be located at a NiO/Ni interface, but rather represent steps on the free NiO surface (cf. Figures 3(g) and 4(e)).

In bulk NiO metal cations have a higher mobility than oxygen anions [37]. Hirth and Mitchell [38] have argued that during nickel oxidation interfacial oxygen remains in the same position and disconnections at the metal/oxide interface are immobile. Instead, nickel diffuses through the oxide towards the external surface where oxidation takes place [39,40]. In this study, however, extensive Ni diffusion is not required as oxidation takes place at the NiO/Ni interface where metallic Ni atoms are available. Instead, the oxidation process is assumed to be governed by oxygen vacancy migration along the NiO/Ni interface plane. Once the metal particle becomes smaller than the oxide crystal, step migration on the surface NiO replaces disconnection motion at the interface and may be characterized by a different migration rate. Such change in migration

rate may cause changes in crystallographic growth direction previously observed during in-situ ESEM experiments [29]. Furthermore, once the in-plane particle radius exceeds its out-of-plane thickness, nickel oxide growth might be dominated by oxygen anion flux through the nickel particle.

Medlin and collaborators [41,42] have recently applied a model by Hirth and Pond [22] to estimate the flux of material required for an interfacial phase transformation. For the oxidation reaction at the Ni/NiO (111) interface observed in Figure 3 the flux of oxygen anions J_0 that is required for ledge movement is estimated by

$$J_{O}\left(\frac{\text{mol}}{\text{m}^{2}\cdot\text{s}}\right) = \frac{I_{O}}{L\cdot\Delta y} = \frac{L\cdot v\cdot (h\Delta X_{O} + b_{n}X_{O}^{Ni})}{L\cdot\Delta y} = \frac{v\cdot (d_{Ni(111)}\Delta X_{O} + b_{n}X_{O}^{Ni})}{\Delta y}.$$
 (1)

 I_0 represents the current of oxygen anions; $d_{(hkl)}$ is the interplanar spacing of the corresponding (hkl) planes. h represents the overlap step height of the disconnection; b_n represents the burgers vector in the direction perpendicular to the interface; X_0 is the number of oxygen atoms per unit volume in a phase ΔX_0 and is the difference between X_0^{Ni} and X_0^{Ni0} ; L represents the length of the ledge; Δy represents the distance a disconnection travels and v represents the step movement velocity. A combination of equation 1 and Fick's First Law was used to estimate the diffusion coefficient for oxygen associated with disconnection movement. According to Fick's first law, the diffusion coefficient of oxygen is calculated to be 1.2×10^{-18} m²/s. This result is in excellent agreement with the effective diffusion coefficient for oxygen in NiO, i.e. 6.2×10^{-18} m²/s [37]. The volume diffusion coefficient of oxygen in NiO is 7.7×10^{-21} m²/s [37], hence corroborating that NiO nanorod growth is governed by oxygen diffusion along the NiO/Ni interface.

The growth process outlined above resembles TLK growth originally proposed by Kossel [13] and Stranski [14] in which adatoms are attached at thermodynamically favorable kink sites, i.e., at steps in projection of the crystal surface. The experimental results presented in this study

expand the TLK model and demonstrate its applicability for reactive crystal growth at buried solid-state heterogeneous interfaces. NiO nanorod growth by NiO/Ni interface migration is accomplished by the consumption of the Ni nanoparticle that serves as reactant for the formation of NiO as the reaction product. The thermodynamic driving force for ledge movement is rooted in the temperature and oxygen partial pressure during the in-situ growth experiments. The growth model may also represent a viable mechanism for the anisotropic growth of NiO nanostructures in water vapor [29]. Unlike previous reports [28] disconnection movement is observed from atomically flat interfaces for which no curvature contributes an additional driving force for interface migration. Calculations of materials flux required for the advancement of disconnections are consistent with oxygen vacancy interface diffusion. The growth model discovered in this study demonstrates the feasibility to apply the existing TLK model to reaction-controlled migration of internal interfaces.

The authors acknowledge financial support from the National Science Foundation [DMR-1836571]. The ESEM was acquired through the NSF-MRI program [DMR-1725618]. The authors appreciate assistance by Dr. Xiaofeng Zhang and Dr. Takeo Kamino (Hitachi High Technologies). Discussions with Dr. Douglas Medlin (Sandia National Laboratories) and Mr. Joseph Wood were invaluable.

References:

- [1] C.M. Lieber, Solid State Commun. 107 (1998) 607–616.
- [2] J. Chen, B.J. Wiley, Y. Xia, Langmuir 23 (2007) 4120–4129.
- [3] Z.L. Wang, ACS Nano 2 (2008) 1987–1992.
- [4] P.M. Rørvik, T. Grande, M.-A. Einarsrud, Adv. Mater. 23 (2011) 4007–4034.
- [5] B. Weng, S. Liu, Z.-R. Tang, Y.-J. Xu, RSC Adv. 4 (2014) 12685–12700.
- [6] R.S. Wagner, W.C. Ellis, Appl. Phys. Lett. 4 (1964) 89–90.

- [7] T.J. Trentler, S.C. Goel, K.M. Hickman, A.M. Viano, M.Y. Chiang, A.M. Beatty, P.C. Gibbons, W.E. Buhro, J. Am. Chem. Soc. 119 (1997) 2172–2181.
- [8] C.-Y. Wen, M.C. Reuter, J. Tersoff, E.A. Stach, F.M. Ross, Nano Lett. 10 (2010) 514–519.
- [9] W.K. Burton, N. Cabrera, F.C. Frank, Nature 163 (1949) 398–399.
- [10] W.K. Burton, N. Cabrera, F.C. Frank, N.F. Mott, Philos. Trans. R. Soc. Lond. Ser. Math. Phys. Sci. 243 (1951) 299–358.
- [11] J. Westwater, D.P.G.D.P. Gosain, S.U.S. Usui, Jpn. J. Appl. Phys. 36 (1997) 6204.
- [12] S.H. Oh, K. van Benthem, S.I. Molina, A.Y. Borisevich, W. Luo, P. Werner, N.D. Zakharov, D. Kumar, S.T. Pantelides, S.J. Pennycook, Nano Lett. 8 (2008) 1016–1019.
- [13] W. Kossel, Nachr. Ges. Wiss. Göttingen 143 (1927).
- [14] I.N. Stranski, Z. Phys. Chem 136 (1928) 259–278.
- [15] S. Hofmann, R. Sharma, C.T. Wirth, F. Cervantes-Sodi, C. Ducati, T. Kasama, R.E. Dunin-Borkowski, J. Drucker, P. Bennett, J. Robertson, Nat. Mater. 7 (2008) 372–375.
- [16] S.A. Morin, M.J. Bierman, J. Tong, S. Jin, Science 328 (2010) 476–480.
- [17] F. Meng, M. Estruga, A. Forticaux, S.A. Morin, Q. Wu, Z. Hu, S. Jin, ACS Nano 7 (2013) 11369–11378.
- [18] S. Jin, M.J. Bierman, S.A. Morin, J. Phys. Chem. Lett. 1 (2010) 1472–1480.
- [19] G.M. Raynaud, R.A. Rapp, Oxid. Met. 21 (1984) 89–102.
- [20] R.L. Tollman, E.A. Gulbransen, J. Electrochem. Soc. 114 (1967) 1227.
- [21] H. Gleiter, Acta Metall. 17 (1969) 565-573.
- [22] J.P. Hirth, R.C. Pond, Acta Mater. 44 (1996) 4749–4763.
- [23] J. Han, S.L. Thomas, D.J. Srolovitz, Prog. Mater. Sci. 98 (2018) 386–476.
- [24] A.H. Heuer, M. Zahiri Azar, Scr. Mater. 102 (2015) 15–18.
- [25] H. Sternlicht, W. Rheinheimer, R.E. Dunin-Borkowski, M.J. Hoffmann, W.D. Kaplan, J. Mater. Sci. 54 (2019) 3694–3709.
- [26] H. Sternlicht, W. Rheinheimer, J. Kim, E. Liberti, A.I. Kirkland, M.J. Hoffmann, W.D. Kaplan, J. Mater. Sci. 54 (2019) 3710–3725.
- [27] H. Sternlicht, W. Rheinheimer, A. Mehlmann, A. Rothschild, M.J. Hoffmann, W.D. Kaplan, Scr. Mater. 188 (2020) 206–211.
- [28] L. Zou, J. Li, D. Zakharov, E.A. Stach, G. Zhou, Nat. Commun. 8 (2017) 307.
- [29] B. Qu, K. van Benthem, J. Am. Ceram. Soc. 105 (2022) 2454–2464.
- [30] K. Koga, M. Hirasawa, Mater. Res. Express 1 (2014) 045021.
- [31] K. Tai, K. Sun, B. Huang, S.J. Dillon, Nanotechnology 25 (2014) 145603.
- [32] K. Sun, J. Xue, K. Tai, S.J. Dillon, Sci. Rep. 7 (2017) 7017.
- [33] T. Kamino, T. Yaguchi, M. Konno, A. Watabe, T. Marukawa, T. Mima, K. Kuroda, H. Saka, S. Arai, H. Makino, Y. Suzuki, K. Kishita, J. Electron Microsc. (Tokyo) 54 (2005) 497–503.
- [34] D.R. Gaskell, D.E. Laughlin, Introduction to the Thermodynamics of Materials, Sixth Edition, CRC Press, 2017.
- [35] B. Qu, K. van Benthem, J. Am. Ceram. Soc. (n.d.).
- [36] L. Chen, W. Lu, C.M. Lieber, (2014) 1–53.
- [37] S. Chevalier, F. Desserrey, J.P. Larpin, Oxid. Met. 64 (2005) 219–234.
- [38] J.P. Hirth, T.E. Mitchell, Acta Mater. 56 (2008) 5701–5707.
- [39] B. Pieraggi, R.A. Rapp, J.P. Hirth, Oxid. Met. 44 (1995) 63–79.
- [40] B. Pieraggi, R.A. Rapp, Acta Metall. 36 (1988) 1281–1289.
- [41] D.L. Medlin, J.D. Sugar, Scr. Mater. 62 (2010) 379–382.
- [42] N.A. Heinz, T. Ikeda, G.J. Snyder, D.L. Medlin, Acta Mater. 59 (2011) 7724–7735.